Journal of Advances in Mathematics and Computer Science

25(1): 1-31, 2017; Article no.JAMCS.36902

Previously known as British Journal of Mathematics & Computer Science
ISSN: 2231-0851

Comparison among Unstructured TVD, ENO and UNO Schemes in Two-dimensions

Edisson Sávio de Góes Maciel[1*] and Cláudia Regina de Andrade[2]

[1]Instituto Tecnológico de Aeronáutica (ITA), Rua Santa Clara, 245 – Cx. Postal: 2029 – 12.243-970, São José dos Campos, SP, Brazil.
[2]Instituto Tecnológico de Aeronáutica (ITA), Praça Mal. Do Ar Eduardo Gomes, 50 – Vila das Acácias, São José dos Campos, SP, Brazil.

Authors' contributions

This work was carried out in collaboration between both authors. Author ESDGM designed the study, performed the statistical analysis, wrote the protocol, wrote the first draft of the manuscript and managed the analyses of the study. Author CRDA managed the literature searches. Both authors read and approved the final manuscript.

Article Information

DOI: 10.9734/JAMCS/2017/36902
Editor(s):
(1) Heng-you Lan, Department of Mathematics, Sichuan University of Science & Engineering, China.
Reviewers:
(1) Sanjib Kumar Datta, University of Kalyani, India.
(2) Grienggrai Rajchakit, Maejo University, Thailand.
(3) Subramaniam Jahanadan, Malaysia.
Complete Peer review History: http://www.sciencedomain.org/review-history/21451

Original Research Article

Received: 22nd September 2017
Accepted: 13th October 2017
Published: 18th October 2017

Abstract

In this work, unstructured TVD, ENO and UNO schemes are applied to solve the Euler equations in two-dimensions. They are implemented on a finite volume context and cell centered data base. The algorithms of Yee, Warming and Harten 1982; Harten; Yee and Kutler; Yee Warming and Harten 1985; Yee; Yee and Harten; Harten and Osher; Yang; Hughson and Beran; and Yang and Hsu are implemented to solve such system of equations in two-dimensions. All schemes are flux difference splitting and good resolution is expected. This study deals with calorically perfect gas model and in so on the cold gas formulation is employed. Two problems are studied, namely: the transonic convergent-divergent symmetrical nozzle, and the supersonic ramp. A spatially variable time step is implemented to accelerate the convergence process. The results highlights the excellent performance of the Yang TVD scheme, yielding an excellent pressure distribution at the nozzle wall, whereas the Harten and Osher scheme yields accurate values to the angle of the oblique shock wave and the best wall pressure distributions in the ramp problem.

**Corresponding author: E-mail: edissonsavio@yahoo.com.br;*

Keywords: *Supersonic and transonic flow; Euler equations; TVD schemes; ENO schemes; UNO schemes; flux difference splitting; two-dimension; second and third-order schemes.*

1 Introduction

Conventional shock capturing schemes for the solution of nonlinear hyperbolic conservation laws are linear and L2-stable (stable in the L2-norm) when considered in the constant coefficient case ([1]). There are three major difficulties in using such schemes to compute discontinuous solutions of a nonlinear system, such as the compressible Euler equations:

(i) Schemes that are second (or higher) order accurate may produce oscillations wherever the solution is not smooth;
(ii) Nonlinear instabilities may develop in spite of the L2-stability in the constant coefficient case;
(iii) The scheme may select a nonphysical solution.

It is well known that monotone conservative difference schemes always converge and that their limit is the physical weak solution satisfying an entropy inequality. Thus monotone schemes are guaranteed to have no difficulties (ii) and (iii). However, monotone schemes are only first order accurate. Consequently, they produce rather crude approximations whenever the solution varies strongly in space or time.

When using a second (or higher) order accurate scheme, some of these difficulties can be overcome by adding a hefty amount of numerical dissipation to the scheme. Unfortunately, this process brings about an irretrievable loss of information that exhibits itself in degraded accuracy and smeared discontinuities. Thus, a typical complaint about conventional schemes which are developed under the guidelines of linear theory is that they are not robust and/or not accurate enough.

To overcome the difficulties, a new class of schemes was considered that is more appropriate for the computation of weak solutions (i.e., solutions with shocks and contact discontinuities) of nonlinear hyperbolic conservation laws. These schemes are required (a) to be total variation diminishing in the nonlinear scalar case and the constant coefficient system case ([2-3]) and (b) to be consistent with the conservation law and an entropy inequality ([4-5]). The first property guarantees that the scheme does not generate spurious oscillations. Schemes with this property are referred in the literature as total variation diminishing (TVD) schemes (or total variation non-increasing, TVNI, [3]). The latter property guarantees that the weak solutions are physical ones. Schemes in this class are guaranteed to avoid difficulties (i)-(iii) mentioned above. Some schemes in this context are mentioned below:

Yee [6] developed a flux difference splitting scheme, which utilizes the concept of TVD ("Total Variation Diminishing"). It utilizes the concept of a modified inviscid flux vector to calculate the numerical fluxes. It utilizes artificial compressibility terms to take into account compressibility effects. The second order of accuracy is obtained with an appropriate definition of the modified numerical flux. The scheme satisfies a proper entropy inequality to ensure that the limit solution will have only physically relevant discontinuities. The scheme presented is second-order accurate in space and time. The time integration is accomplished by a Runge-Kutta method.

Harten [3] defined a class of new explicit second-order accurate finite difference schemes, for the computation of weak solutions of hyperbolic conservation laws. The highly non-linear schemes were obtained by applying a non-oscillatory first-order accurate scheme to an appropriately modified flux function. The so-derived second-order accurate schemes achieve high resolution while preserving the robustness of the original non-oscillatory first-order accurate scheme. These schemes are called TVD ("Total Variation Diminishing") ones and yield physically relevant solutions by the use of an entropy condition. Our implementation of the [3] scheme is accomplished on a finite volume context. The scheme presented is second-order accurate in space. The time integration is accomplished by a Runge-Kutta method, second-order accurate in time.

Yee and Kutler [7] emphasized that a one-parameter family of explicit and implicit second order accurate, entropy satisfying, total variation diminishing (TVD) schemes had been developed by [3]. These schemes had the property of not generating spurious oscillations for one-dimensional non-linear scalar hyperbolic conservation laws and constant coefficient hyperbolic systems. Application of these methods to one- and two-dimensional fluid flows containing shocks (in Cartesian coordinates) yielded highly accurate non-oscillatory numerical solutions. The goal of the work of [7] was to extend these methods to the multidimensional Euler equations in generalized coordinate systems. The scheme is second order accurate in space and time. The time integration is accomplished by a Runge-Kutta method, second-order accurate.

Yee et al. [8] applied a new implicit unconditionally stable high resolution TVD scheme to steady state calculations. It was a member of a one-parameter family of explicit and implicit second order accurate schemes developed by [3] for the computation of weak solutions of one-dimensional hyperbolic conservation laws. The scheme was guaranteed not to generate spurious oscillations for a nonlinear scalar equation and a constant coefficient system. Numerical experiments have shown that the scheme not only had a fairly rapid convergence rate, but also generated a highly resolved approximation to the steady state solution. A detailed implementation of the implicit scheme for the one- and two-dimensional compressible inviscid equations of gas dynamics was presented. Some numerical experiments of one- and two-dimensional fluid flows containing shocks demonstrated the efficiency and accuracy of the new scheme.

Yee [9] reformulated a one-parameter family of second-order explicit and implicit total variation diminishing (TVD) schemes so that a simpler and wider group of limiters was included. The resulting scheme can be viewed as a symmetrical algorithm with a variety of numerical dissipation terms that were designed for weak solutions of hyperbolic problems. This was a generalization of the works of Roe and Davis to a wider class of symmetric schemes other than Lax-Wendroff. The main properties of this class of schemes were that they could be implicit, and, when steady-state calculations were sought, the numerical solution was independent of the time step. Numerical experiments with two-dimensional unsteady and steady-state airfoil calculations have shown that the proposed symmetric TVD schemes were quite robust and accurate. In the present study, only the results with the Minmod limiter, Eq. (44), are presented.

Yee and Harten [10] considered that Harten's method of constructing high resolution TVD schemes involves starting with a first-order TVD scheme and applying it to a modified flux. The modified flux is chosen so that the scheme is second-order at regions of smoothness and first-order at points of extrema. This technique is sometimes referred to as the modified flux approach. [10] extended a TVD scheme (via the modified flux approach) to generalized coordinate systems and discussed the various solution strategies for the implicit TVD schemes for more efficient two-dimensional steady-state applications. The TVD scheme was initially an implicit TVD one developed to solve a two-dimensional gas-dynamic problem in Cartesian coordinate.

Hughson and Beran [11] presented an explicit, second order accurate, total variation diminishing (TVD) scheme applied to the Euler equations in axisymmetric form to study hypersonic blunt-body flows. The modified flux function approach of [3], with modification by [12], for two-dimensional flows is extended to treat axisymmetric flows. The scheme was presented on a finite difference context, but in our implementation, the scheme is written on a finite volume context. Roe's averaging for a perfect gas was used to assess the eigenvalues and eigenvectors at cell interfaces, because it has the computational advantage of resolving stationary discontinuities. An entropy condition is implemented to assure relevant physical solutions. Linear and non-linear limiters (g's functions) assure second order accuracy as well control the amount of numerical dissipation added to the flow equations.

Recently, a new class of uniformly high order accurate essentially nonoscillatory (ENO) schemes have been developed by [13-16]. They presented a hierarchy of uniformly high order accurate schemes that generalize [17]'s scheme, its second order accurate MUSCL extension ([18-19]), and the total variation diminishing (TVD) scheme ([3]) to arbitrary order of accuracy. In contrast to the earlier second order TVD schemes which drop to first order accuracy at local extrema and maintain second order accuracy in smooth regions, the new ENO schemes are uniformly high order accurate throughout, even at critical points. The ENO schemes use a reconstruction algorithm that is derived from a new interpolation technique that when applied

to piecewise smooth data gives high order accuracy whenever the function is smooth but avoids a Gibbs phenomenon at discontinuities. An adaptive stencil of grid points is used; therefore, the resulting schemes are highly nonlinear even in the scalar case. Some schemes constructed in this way were:

Harten and Osher [13] presented a hierarchy of uniformly high order accurate schemes that generalize [17] scheme, and its second order accurate extension of monotonic upstream schemes for conservation laws (MUSCL) ([18-19]) and total variation diminishing (TVD) schemes ([3] and [20]) to arbitrary order of accuracy.

Yang [21] has presented two time level explicit and implicit finite difference shock capturing schemes based on the characteristic flux difference splitting method and the modified flux approach with the essentially nonoscillatory (ENO) property that [13] have been developed for the two-dimensional Euler equations. The methods were conservative, uniformly second order accurate in time and space, even at local extrema. General coordinate systems were used to treat complex geometries. Standard alternating direction implicit approximate factorization was used for constructing implicit schemes. Numerical results have been obtained for unsteady shock wave reflection around general two-dimensional blunt body and for steady transonic flows over a circular arc bump in a channel. Properties of ENO schemes as applied to two-dimensional flows with multiple embedded discontinuities were discussed. Comparisons of the performance between the presented ENO schemes and author's previous total variation diminishing schemes were also included. The [21] scheme could be ENO or TVD ones depending of the choice of a free parameter.

Yang [22] developed high-resolution explicit finite difference nonoscillatory shock-capturing schemes based on Harten's essentially nonoscillatory interpolation using reconstruction via primitive function approach with N = 3 for simulating unsteady compressible flow. The extension to nonlinear system is done using Roe's method, which permits the use of different scalar schemes for different characteristic fields. For multidimensional problems, a Runge-Kutta scheme was adopted. Numerical simulations of unsteady shock diffraction by an elliptic cylinder and shock wave propagating through a convergent-divergent nozzle were studied in their original paper.

In this work, the Euler equations in two-dimensions are solved by the use of TVD, ENO and UNO schemes, second and third order accurate. The following ten flux difference splitting algorithms are employed: [6, 3, 7-11], on a TVD approach and [13,21], on an ENO approach, and finally [22], on a UNO approach. A finite volume formulation is employed on conservative and unstructured contexts. The time discretization employs a Runge-Kutta method of five steps. All ten algorithms are applied to the solution of two problems: the transonic convergent-divergent nozzle, and the supersonic ramp. All schemes are accelerated to the steady state solution using a spatially variable time step procedure, which has proved excellent characteristics of convergence [23-24]. The results have demonstrated that the best result of the wall pressure distribution in the nozzle case is due to [21] and the best wall pressure distribution and shock angle in the ramp case is due to [13] in both TVD and ENO variants.

The motivation of the paper is to construct unstructured solutions to perfect gas formulation aiming their application in "hot gas" flows. The present work is a first step in extending unstructured strategy to chemical and thermochemical non-equilibrium flows using ENO or spectral methods. The implementation of the unstructured strategy to two-dimensional thermochemical non-equilibrium formulation using spectral methods is almost ready. The results in the present paper are very encouraging and the use of such discretization in spectral methods is ready to be used.

The results of the present paper are meaningful in the sense that with unstructured discretization more complex problems can be addressed and the intention of the present authors is to study complex unstructured three-dimensional problems, like wings, fuselage, etc. In two-dimensions, we can explore the advantage of using triangular cells that conforms to the geometry under study better than rectangular cells, mainly no very close to the geometry, where rectangular cells are the best, but close to the bulk flow. The results in this paper are an indicative that unstructured discretization is better for complex configurations than the structured discretization. In relation to structured solutions, the use of Quimera or multi-block meshes are

needed for solve complex configurations. In the unstructured solutions, these procedures are not necessary. So, in relation to structured solutions, the unstructured discretization is far superior.

2 Euler Equations

The fluid movement is described by the Euler equations, which express the conservation of mass, of linear momentum and of energy to an inviscid medium, heat non-conductor and compressible, in the absence of external forces. In integral and conservative forms, these equations can be given by:

$$\partial/\partial t \int_V Q dV + \int_S \left[(E_e) n_x + (F_e) n_y \right] dS = 0, \tag{1}$$

with Q written to a Cartesian system, V is the cell volume, n_x and n_y are the components of the normal unity vector to the flux face, S is the flux area, and E_e and F_e are the convective flux vector components. The Q, E_e and F_e vectors are represented by:

$$Q = \begin{Bmatrix} \rho \\ \rho u \\ \rho v \\ e \end{Bmatrix}, \quad E_e = \begin{Bmatrix} \rho u \\ \rho u^2 + p \\ \rho uv \\ (e+p)u \end{Bmatrix} \quad \text{and} \quad F_e = \begin{Bmatrix} \rho v \\ \rho uv \\ \rho v^2 + p \\ (e+p)v \end{Bmatrix}, \tag{2}$$

being ρ the fluid density; u and v the Cartesian components of the velocity vector in the x and y directions, respectively; e the total energy; and p the static pressure of the fluid medium.

In the studied problems, the Euler equations were nondimensionalized in relation to the freestream density, ρ_∞, and in relation to the freestream speed of sound, a_∞. Hence, the density is nondimensionalized in relation to ρ_∞; the u and v velocity components are nondimensionalized in relation to a_∞; and the pressure and the total energy are nondimensionalized in relation to the product $\rho_\infty(a_\infty)^2$. The matrix system of the Euler equations is closed with the state equation $p = (\gamma - 1)\left[e - 0.5\rho(u^2 + v^2) \right]$, assuming the ideal gas hypothesis. The total enthalpy is determined by $H = (e + p)/\rho$.

Equation (1) describes a relation in which the time rate of variation of the Q state vector, inside a V volume, is balanced by the net convective flux which crosses the S boundary surface. The calculation domain is divided in a great number of triangular cells and the Eq. (1) is applied to each cell.

3 Yee, Warming and Harten (1982) TVD Algorithm

The [6] algorithm, second order accurate in space, is specified by the determination of the numerical flux vector at "l" interface.

Following a finite volume formalism, which is equivalent to a generalized coordinate system, the right and left cell volumes, as well the interface volume, necessary to a coordinate change, are defined by:

$$V_R = V_{ne}, \quad V_L = V_i \quad \text{and} \quad V_l = 0.5(V_R + V_L), \tag{3}$$

where "R" and "L" represent right and left states, respectively, and "ne" represent a neighbor volume to the "i" volume. In this work, it was adopted that "L" is associated to properties of a given "i" volume and "R" is

associated to properties of the "ne" neighbor volume. The cell volume on an unstructured context is defined by:

$$V_i = 0.5\left|\left(x_{n1}y_{n2} + y_{n1}x_{n3} + x_{n2}y_{n3}\right) - \left(x_{n3}y_{n2} + y_{n3}x_{n1} + x_{n2}y_{n1}\right)\right|, \tag{4}$$

with n1, n2 and n3 being the nodes of a given triangular cell. The description of the computational cell and its nodes, flux interfaces and neighbors are shown in Fig. 1.

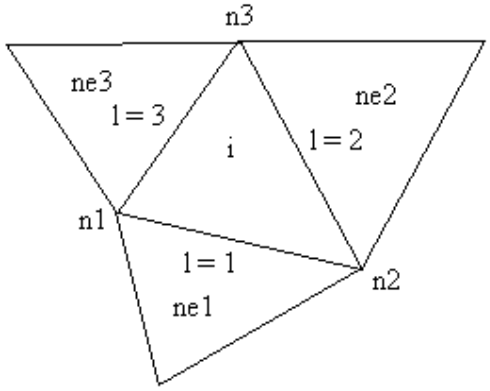

Fig. 1. Unstructured cell with its defined nodes and flux interfaces.

The area components at the "l" interface are defined by:

$$S_x^l = n_x^l S^l \quad \text{and} \quad S_y^l = n_y^l S^l, \tag{5}$$

where n_x^l, n_y^l and S_l are defined as:

$$n_x^l = \Delta y_l / \left(\Delta x_l^2 + \Delta y_l^2\right)^{0.5},\ n_y^l = -\Delta x_l / \left(\Delta x_l^2 + \Delta y_l^2\right)^{0.5} \text{ and } S^l = \left(\Delta x_l^2 + \Delta y_l^2\right)^{0.5}. \tag{6}$$

Expressions to Δx_l and Δy_l are given in Tab. 1. The metric terms to this generalized coordinate system are defined as:

Table 1. Values of Δx_l and Δy_l.

Interface	Δx_l	Δy_l
l = 1	$x_{n2} - x_{n1}$	$y_{n2} - y_{n1}$
l = 2	$x_{n3} - x_{n2}$	$y_{n3} - y_{n2}$
l = 3	$x_{n1} - x_{n3}$	$y_{n1} - y_{n3}$

$$h_x = S_x^l / V_l,\ h_y = S_y^l / V_l \quad \text{and} \quad h_n = S^l / V_l. \tag{7}$$

The properties calculated at the flux interface are obtained by arithmetical average or by Roe average. In the present work, the Roe average was used:

$$\rho_l = \sqrt{\rho_R \rho_L}\,,\ u_l = \frac{u_R\sqrt{\rho_R} + u_L\sqrt{\rho_L}}{\sqrt{\rho_R} + \sqrt{\rho_L}},\ v_l = \frac{v_R\sqrt{\rho_R} + v_L\sqrt{\rho_L}}{\sqrt{\rho_R} + \sqrt{\rho_L}} \quad \text{and}$$

$$H_l = \frac{H_R\sqrt{\rho_R} + H_L\sqrt{\rho_L}}{\sqrt{\rho_R} + \sqrt{\rho_L}}; \tag{8}$$

$$a_l = \sqrt{(\gamma - 1)\left[H_l - 0.5\left(u_l^2 + v_l^2\right)\right]}, \tag{9}$$

where a_l is the speed of sound at the flux interface. The eigenvalues of the Euler equations, in the normal direction to the flux face, to the convective flux are given by:

$$q_{normal} = u_l h_x + v_l h_y\,,\ \lambda_1 = q_{normal} - a_l h_n\,,\ \lambda_2 = \lambda_3 = q_{normal} \quad \text{and} \quad \lambda_4 = q_{normal} + a_l h_n\,. \tag{10}$$

The jumps of the conserved variables, necessary to the construction of the [6] dissipation function, are given by:

$$\Delta e = V_l\left(e_R - e_L\right),\ \Delta\rho = V_l\left(\rho_R - \rho_L\right),\ \Delta(\rho u) = V_l\left[(\rho u)_R - (\rho u)_L\right] \text{ and } \Delta(\rho v) = V_l\left[(\rho v)_R - (\rho v)_L\right]; \tag{11}$$

The α vectors to the "l" interface are calculated by the following expressions:

$$\alpha^1 = 0.5(aa - bb),\ \alpha^2 = \Delta\rho - aa\,,\ \alpha^3 = cc \quad \text{and} \quad \alpha^4 = 0.5(aa + bb), \tag{12}$$

with:

$$aa = {(\gamma - 1)}\Big/{a_l^2}\left[\Delta e + 0.5\left(u_l^2 + v_l^2\right)\Delta\rho - u_l\Delta(\rho u) - v_l\Delta(\rho v)\right]; \tag{13}$$

$$bb = {1}\Big/{a_l}\left[h_x'\Delta(\rho u) - \left(h_x' u_l + h_y' v_l\right)\Delta\rho + h_y'\Delta(\rho v)\right]; \tag{14}$$

$$cc = h_x'\Delta(\rho v) + \left(h_{\dot{y}}' u_l - h_x' v_l\right)\Delta\rho - h_y'\Delta(\rho u); \tag{15}$$

$$h_x' = h_x/h_n \quad \text{and} \quad h_y' = h_y/h_n\,. \tag{16}$$

The [6] dissipation function uses the right-eigenvector matrix of the normal to the flux face Jacobian matrix in generalized coordinates:

$$R_l = \begin{bmatrix} 1 & 1 & 0 & 1 \\ u_l - h_x' a_l & u_l & -h_y' & u_l + h_x' a_l \\ v_l - h_y' a_l & v_l & h_x' & v_l + h_y' a_l \\ H_l - h_x' u_l a_l - h_y' v_l a_l & 0.5\left(u_l^2 + v_l^2\right) & h_x' v_l - h_y' u_l & H_l + h_x' u_l a_l + h_y' v_l a_l \end{bmatrix}. \tag{17}$$

Two options to the ψ_m entropy function, responsible to guarantee that only relevant physical solutions are to be considered, are implemented aiming an entropy satisfying algorithm:

$$\nu_m = \Delta t\lambda_m = Z_m \quad \text{and} \quad \psi_m = Z_m^2 + 0.25\,; \tag{18}$$

Or:

$$\psi_m = \begin{cases} |Z_m|, & \text{if } |Z_m| \geq \delta_f \\ 0.5\left(Z_m^2 + \delta_f^2\right)\Big/\delta_f, & \text{if } |Z_m| < \delta_f \end{cases}, \tag{19}$$

where "m" varies from 1 to 4 (two-dimensional space) and δ_f assuming values between 0.1 and 0.5, being 0.2 the recommended value by [6]. In the present studies, Eq. (18) was used to perform the numerical experiments.

The $\tilde{g}$ function at the "l" interface is defined by:

$$\tilde{g}_i^m = 0.5\left(\psi_m - Z_m^2\right)\alpha_i^m\,. \tag{20}$$

The g numerical flux function, which is a limited function to avoid the formation of new extremes in the solution and is responsible to the second order accuracy of the scheme, is given by:

$$g_i^m = \text{signal}_m \times \text{MAX}\left(0.0; \text{MIN}\left(\left|\tilde{g}_i^m\right|, \tilde{g}_{i-1}^m \times \text{signal}_m\right)\right), \tag{21}$$

where signal_m is equal to 1.0 if $\tilde{g}_i^m \geq 0.0$ and -1.0 otherwise.

The θ term, responsible to the artificial compressibility, as referred in the CFD community, which enhances the resolution of the scheme at discontinuities, is defined as follows:

$$\theta_i^m = \begin{cases} \left|\alpha_i^m - \alpha_{i-1}^m\right|\Big/\left(\left|\alpha_i^m\right| + \left|\alpha_{i-1}^m\right|\right), & \text{if } \left|\alpha_i^m\right| + \left|\alpha_{i-1}^m\right| \neq 0.0 \\ 0.0, & \text{if } \left|\alpha_i^m\right| + \left|\alpha_{i-1}^m\right| = 0.0 \end{cases}; \tag{22}$$

The β vector at the "l" interface, which introduces the artificial compression term in the algorithm, is defined by the following expression:

$$\beta_m = 1.0 + \omega_m \text{MAX}(\theta_i^m, \theta_{i+1}^m)\,, \tag{23}$$

where ω_m assumes the following values: $\omega_1 = 0.25$ (non-linear field), $\omega_2 = \omega_3 = 1.0$ (linear field) and $\omega_4 = 0.25$ (non-linear field).

The numerical characteristic speed, φ_m, at the "l" interface, which is responsible to transport the numerical information associated to the g numerical flux function, is defined by:

$$\varphi_m = \begin{cases} \left(g_{i+1}^m - g_i^m\right)\Big/\alpha^m, & \text{if } \alpha^m \neq 0.0 \\ 0.0, & \text{if } \alpha^m = 0.0 \end{cases}. \tag{24}$$

The entropy function is redefined considering φ_m and β_m: $Z_m = \nu_m + \beta_m\varphi_m$, and ψ_m is recalculated according to Eq. (18) or to Eq. (19). Finally, the [6] dissipation function, to second order accuracy in space, is constructed by the following matrix-vector product:

$$\{D_{YWH82}\}_l = [R]_l \left\{ \left(\beta(g_i + g_{i+1}) - \psi\alpha\right) \Big/ \Delta t_i \right\}_l . \tag{25}$$

The convective numerical flux vector to the "l" interface is described by:

$$VF_l^{(m)} = \left(E_l^{(m)} h_x + F_l^{(m)} h_y\right) V_l + 0.5 D_{YWH}^{(m)}, \tag{26}$$

with:

$$E_l^{(m)} = 0.5\left(E_R^{(m)} + E_L^{(m)}\right) \quad \text{and} \quad F_l^{(m)} = 0.5\left(F_R^{(m)} + F_L^{(m)}\right). \tag{27}$$

The time integration is performed by an explicit method, second order accurate, Runge-Kutta type of five stages and can be represented of generalized form by:

$$\begin{aligned} Q_i^{(0)} &= Q_i^{(n)} \\ Q_i^{(k)} &= Q_i^{(0)} - \alpha_k \, \Delta t_i / V_i \times C\left(Q_i^{(k-1)}\right), \\ Q_i^{(n+1)} &= Q_i^{(k)} \end{aligned} \tag{28}$$

with k = 1, 2; $\alpha_1 = 1/2$, and $\alpha_2 = 1$. The contribution of the convective numerical flux vectors is determined by the C_i vector:

$$C_i^{(m)} = VF_1^{(m)} + VF_2^{(m)} + VF_3^{(m)}. \tag{29}$$

4 Harten (1983) TVD Algorithm

The [3] algorithm, second order accurate in space, follows the Eqs. (3) to (17). The next step is the definition of the entropy condition, which is defined by Eq. (18), ν_m, and Eq. (19).

The $\tilde{g}$ function at the "l" interface is defined according to Eq. (20) and the g numerical flux function is given by Eq. (21). The numerical characteristic speed φ_m at the "l" interface is defined according to Eq. (24).

The entropy function is redefined considering φ_m: $Z_m = \nu_m + \varphi_m$, and ψ_m is recalculated according to Eq. (19). Finally, the [3] dissipation function, to second order spatial accuracy, is constructed by the following matrix-vector product:

$$\{D_{Harten}\}_l = [R]_l \{(g_i + g_{i+1} - \psi\alpha)/\Delta t_i\}_l . \tag{30}$$

Equations (26), (27) and (29) are used to conclude the numerical flux vector of the [3] scheme and the time integration is performed by the Runge-Kutta method defined by Eq. (28).

5 Yee and Kutler (1985) TVD Algorithm

The [7] algorithm, second order accurate in space, follows Eqs. (3) to (17). The next step consists in determining the θ function. This function is defined in terms of the differences of the gradients of the

characteristic variables to take into account discontinuities effects and is responsible to artificial compression:

$$\theta_i^m = \begin{cases} \dfrac{\left|\alpha_i^m - \alpha_{i-1}^m\right|}{\alpha_i^m + \alpha_{i-1}^m}, & \text{if } \left(\alpha_i^m + \alpha_{i-1}^m\right) \neq 0.0 \\ 0.0, & \text{if } \left(\alpha_i^m + \alpha_{i-1}^m\right) = 0.0 \end{cases}. \tag{31}$$

The κ function at the "l" interface is defined as follows:

$$\kappa_m = 1/8\left(1 + \omega_m \mathrm{MAX}\left(\theta_i^m, \theta_{i+1}^m\right)\right), \tag{32}$$

The g numerical flux function is determined by:

$$g_i^m = \mathrm{signal}_m \times \mathrm{MAX}\left(0.0; \mathrm{MIN}\left(\left|\alpha_i^m\right|, \alpha_{i-1}^m \times \mathrm{signal}_m\right)\right), \tag{33}$$

where signal_m assumes value 1.0 if $\alpha_i^m \geq 0.0$ and -1.0 otherwise. The numerical characteristic speed φ_m at the "l" interface is calculated by the following expression:

$$\varphi_m = \begin{cases} \kappa_m \left(g_{i+1}^m - g_i^m\right)/\alpha^m, & \text{if } \alpha^m \neq 0.0 \\ 0.0, & \text{if } \alpha^m = 0.0 \end{cases}. \tag{34}$$

The ψ_l entropy function at the "l" interface is defined by:

$$\psi_m = \left(\nu_m + \varphi_m\right)^2 + 0.25, \tag{35}$$

with ν_m defined according to Eq. (18). Finally, the [7] dissipation function, to second order spatial accuracy, is constructed by the following matrix-vector product:

$$\left\{D_{\mathrm{Yee/Kutler}}\right\}_l = \left[R\right]_l \left\{\left(\kappa\left(g_i + g_{i+1}\right) - \psi\alpha\right)/\Delta t_i\right\}_l. \tag{36}$$

Equations (26), (27) and (29) are used to conclude the numerical flux vector of [7] scheme and the time integration is performed by the Runge-Kutta method defined by Eq. (28).

6 Yee, Warming and Harten (1985) TVD Algorithm

The [8] algorithm, second order accurate in space, follows Eqs. (3) to (17). The next step is to calculate the numerical flux function, g. The g numerical flux function, which is a limited function to avoid the formation of new extrema in the solution and is responsible to the second order accuracy of the scheme, is given by:

$$g_i^m = \mathrm{signal}_m \times \mathrm{MAX}\left[0.0; \left(\sigma_i^m \left|\alpha_i^m\right|, \mathrm{signal}_m \times \sigma_{i-1}^m \alpha_{i-1}^m\right)\right], \tag{37}$$

where signal_m is equal to 1.0 if $\alpha_i^m \geq 0.0$ and -1.0 otherwise; $\sigma_l\left(\lambda_l\right) = 0.5 Q_l\left(\lambda_l\right)$; and Q is given by:

$$Q_m\left(Z_m\right) = \begin{cases} \left|Z_m\right|, & \text{if } \left|Z_m\right| \geq \delta_f \\ 0.5\left(Z_m^2 + \delta_f^2\right)/\delta_f, & \text{if } \left|Z_m\right| < \delta_f \end{cases}, \tag{38}$$

where "m" varies from 1 to 4 (two-dimensional space) and δ_f assumes values between 0.1 and 0.5, being 0.2 the value recommended by [8]. The θ term, responsible to the artificial compression, which enhances the resolution of the scheme at discontinuities like shock waves and contact discontinuities, is defined as:

$$\theta_i^m = \begin{cases} \left|\alpha_i^m - \alpha_{i-1}^m\right| \Big/ \left(\left|\alpha_i^m\right| + \left|\alpha_{i-1}^m\right|\right), & \text{if } \left|\alpha_i^m\right| + \left|\alpha_{i-1}^m\right| \neq 0.0; \\ 0.0, & \text{if } \left|\alpha_i^m\right| + \left|\alpha_{i-1}^m\right| = 0.0. \end{cases} \tag{39}$$

The β parameter at the l interface, which introduces the artificial compression term, is given by:

$$\beta_i = 1.0 + \omega_i \theta_i^m, \tag{40}$$

in which ω_l assumes the following values: $\omega_1 = 0.25$ (non-linear field), $\omega_2 = \omega_3 = 1.0$ (linear field) and $\omega_4 = 0.25$ (non-linear field). The $\tilde{g}$ function is defined by:

$$\tilde{g}_i^m = \beta_i g_i^m. \tag{41}$$

The numerical characteristic speed, φ_l, at the l interface, which is responsible to transport the numerical information associated to the g numerical flux function, or indirectly through $\tilde{g}$, is defined by:

$$\varphi_m = \begin{cases} \left(\tilde{g}_{i+1}^m - \tilde{g}_i^m\right) \Big/ \alpha^m, & \text{if } \alpha^m \neq 0.0; \\ 0.0, & \text{if } \alpha^m = 0.0. \end{cases} \tag{42}$$

Finally, the [8] dissipation function, to second order of spatial accuracy, is constructed by the following matrix-vector product:

$$\left\{D_{YWH85}\right\}_l = \left[R\right]_l \left\{\left(g_i + g_{i+1}\right) - Q(\lambda + \varphi)\alpha\right\}_l. \tag{43}$$

The convective numerical flux vector to the "l" interface is described by Eqs. (26), (27) and (29) and the time integration is performed by Eq. (28).

7 Yee (1987) TVD Symmetrical Algorithm

The [9] symmetrical algorithm, second order accurate in space, follows Eqs. (3) to (17). The next step is to calculate the entropy function. It is determined by Eq. (19) using the eigenvalues, Eq. (10), of the Euler equations as variables. After that, the Q function is determined. In the present work, five options were implemented. They are:

$$Q(r^-, r^+) = \min \operatorname{mod}(1, r^-) + \min \operatorname{mod}(1, r^+) - 1; \tag{44}$$

$$Q(r^-, r^+) = \min \operatorname{mod}(1, r^-, r^+); \tag{45}$$

$$Q(r^-, r^+) = \min \operatorname{mod}[2, 2r^-, 2r^+, 0.5(r^- + r^+)]; \tag{46}$$

$$Q(r^-, r^+) = \max\{0, \min(2r^-, 1), \min(r^-, 2)\} + \max\{0, \min(2r^+, 1), \min(r^+, 2)\} - 1; \tag{47}$$

$$Q(r^-, r^+) = \frac{r^- + |r^-|}{1 + r^-} + \frac{r^- + |r^+|}{1 + r^+} - 1. \tag{48}$$

Normally the "minmod" function of two arguments is defined as

$$\min \mathrm{mod}(x, y) = sign(x).\max\{0, \min[|x|, y.sign(x)]\}; \tag{49}$$

and the argument r is defined as:

$$r^- = \frac{\alpha_{i-1}^m}{\alpha_i^m} \qquad and \qquad r^+ = \frac{\alpha_{i+1}^m}{\alpha_i^m} \tag{50}$$

Finally, the dissipation operator at the interface "l" is defined as:

$$\{D_{Yee}\}_l = [R]_l \{\psi(\lambda_l)(1 - Q_l)\alpha_l\} \tag{51}$$

and the numerical flux vector is given by:

$$\mathrm{VF}_l^{(m)} = \left(\mathrm{E}_l^{(m)} \mathrm{h}_x + \mathrm{F}_l^{(m)} \mathrm{h}_y\right) \mathrm{V}_l - 0.5 \mathrm{D}_{\mathrm{Yee}}^{(m)}, \tag{52}$$

The time integration is performed by Eq. (28).

8 Yee and Harten (1987) TVD Algorithm

The [10] symmetrical algorithm, second order accurate in space, follows Eqs. (3) to (17). The next step is the determination of the g numerical speed of propagation of information:

$$g_i^m = S \cdot \max[0, \min(|\lambda_l|, S \cdot \alpha_{i-1}^m)\}, where: S = sign(\alpha_i^m). \tag{53}$$

The entropy function is defined by Eq. (19) and the numerical speed of information propagation is determined by:

$$\gamma_i^m = \frac{1}{2}\psi(\lambda_l) \cdot \begin{cases} \left(g_{i+1}^m - g_i^m\right) / \alpha^m, & if \quad \alpha^m \neq 0.0 \\ 0.0, & otherwise \end{cases}. \tag{54}$$

The numerical characteristic speed, φ, is expressed by:

$$\varphi_m = \frac{1}{2}\psi(\lambda_l)(g_i + g_{i+1}) - \psi(\lambda_l + \gamma_i^m)\alpha^m \tag{55}$$

Finally, the [10] dissipation function, to second order of spatial accuracy, is constructed by the following matrix-vector product:

$$\left\{D_{Yee/\,Harten}\right\}_l = \left[R\right]_l \left\{\varphi_m\right\}_l \tag{56}$$

and Eqs. (26), (27), (29) and (28) are used to determine the dissipation operator and accomplish the time integration of the [9] scheme.

9 Hughson and Beran (1991) TVD Algorithm

The [11] algorithm, second order accurate in space, follows the Eqs. (3) to (17). The next step consists in determining the g numerical flux function. To non-linear fields (m = 1 and 4), it is possible to write:

$$g_i^m = \begin{cases} \dfrac{\alpha_i^m \alpha_{i-1}^m + \left|\alpha_i^m \alpha_{i-1}^m\right|}{\alpha_i^m + \alpha_{i-1}^m}, & \text{if } \left(\alpha_i^m + \alpha_{i-1}^m\right) \neq 0.0 \\ 0.0, & \text{if } \left(\alpha_i^m + \alpha_{i-1}^m\right) = 0.0 \end{cases}. \tag{57}$$

To linear fileds (m = 2 and 3), it is possible to write:

$$g_i^m = \text{signal}_m \times \text{MAX}\left(0.0; \text{MIN}\left(\left|\alpha_{i-1}^m\right|, \alpha_i^m \times \text{signal}_m\right)\right), \tag{58}$$

where signal_m assumes the value 1.0 if $\alpha_{i-1}^m \geq 0.0$ and -1.0 otherwise. After that, the Eqs. (18) and (19) are employed and the σ_m term is defined at the "l" interface as:

$$\sigma_m = 0.5\left(\psi_m - Z_m^2\right). \tag{59}$$

The φ_m numerical characteristic speed at the "l" interface is defined by:

$$\varphi_m = \begin{cases} \sigma_m \left(g_{i+1}^m - g_i^m\right) \big/ \alpha^m, & \text{if } \alpha^m \neq 0.0 \\ 0.0, & \text{if } \alpha^m = 0.0 \end{cases}. \tag{60}$$

The entropy function is redefined considering φ_m: $Z_m = \nu_m + \varphi_m$ and ψ_m is recalculated according to Eq. (19). Finally, the [11] dissipation function, to second order accurate in space, is constructed by the following matrix-vector product:

$$\left\{D_{\text{Hughson / Beran}}\right\}_l = \left[R\right]_l \left\{\left[\sigma\left(g_i + g_{i+1}\right) - \psi\alpha\right] \big/ \Delta t_i\right\}_l. \tag{61}$$

After that, Eqs. (26), (27) and (29) are used to conclude the numerical flux vector of the [11] scheme and Eq. (28) is employed to perform the time integration.

10 Harten and Osher (1987) TVD/ENO Algorithm

The [13] algorithm, second order accurate in space, employs Eqs. (3-17). The next step consists in constructing the TVD/ENO numerical flux vector. Initially, it is necessary to define the σ parameter at the "l" interface to calculate the numerical velocity of information propagation, which contributes to the second order spatial accuracy of the scheme:

$$\sigma(z) = 0.5\left[\Psi(z) - \Delta t_i z^2\right]; \tag{62}$$

with Ψ(z) defined according to Eq. (19) and z defined as the eigenvalues at the interface, Eq. (10). The non-linear limited flux function, based on the idea of a modified flux function of [3], is constructed by:

$$\overline{\beta}_i^m = m\left[\alpha_i^m - \zeta\overline{m}\left(\Delta_+\alpha_i^m, \Delta_-\alpha_i^m\right), \alpha_{i-1}^m + \zeta\overline{m}\left(\Delta_+\alpha_{i-1}^m, \Delta_-\alpha_{i-1}^m\right)\right], \tag{63}$$

where the m and $\overline{m}$ limiters are defined as:

$$m(y,z) = \begin{cases} s \times MIN(|y|,|z|), & \text{if } signal(y) = signal(z) = s \\ 0, & \text{otherwise} \end{cases}; \tag{64}$$

$$\overline{m}(y,z) = \begin{cases} y, & \text{if } |y| \le |z| \\ z, & \text{if } |y| > |z| \end{cases}; \tag{65}$$

and the forward and backward operators are defined according to:

$$\Delta_+ = (\cdot)_{i+1} - (\cdot)_i \quad \text{and} \quad \Delta_- = (\cdot)_i - (\cdot)_{i-1}. \tag{66}$$

The numerical velocity of information propagation is calculated by:

$$\overline{\gamma}_i^m = \sigma\left(\lambda_i^m\right)\begin{cases} \left(\overline{\beta}_{i+1}^m - \overline{\beta}_i^m\right)/\alpha^m, & \text{if } \alpha^m \neq 0; \\ 0, & \text{otherwise.} \end{cases} \tag{67}$$

The dissipation function to the TVD and ENO versions of the [13] scheme is defined as:

$$\left(\phi_i^m\right)_{HO} = \sigma\left(\lambda_i^m\right)\left(\overline{\beta}_i^m + \overline{\beta}_{i+1}^m\right) - \Psi\left(\lambda_i^m + \overline{\gamma}_i^m\right)\alpha_i^m, \tag{68}$$

with: "l" assuming values from 1 to 4 (two-dimensional space), ε assuming the value 0.2 recommended by [13], Ψ is the entropy function to guarantee that only relevant physical solutions are admissible, and ζ assumes the value 0.0 to obtain the TVD scheme of [3], second order accurate, and 0.5 to obtain the essentially non-oscillatory scheme, uniform second order accuracy in the field, of [13].

Finally, the dissipation operator of [13], to second order of spatial accuracy, in its TVD and ENO versions, is constructed by the following matrix-vector product:

$$\left\{D_{Harten/Osher}\right\}_l = \left[R\right]_l \left\{\phi_{HO}\right\}_l. \tag{69}$$

The complete numerical flux vector to the "l" interface is described by Eqs. (26), (27), and (29) whereas the tine integration is performed by the Runge-Kutta method of Eq. (28).

11 Yang (1990) TVD/ENO Algorithm

11.1 Explicit upwind algorithm

A typical conservative numerical scheme, using a finite volume and unstructured formulations, for solving Eq. (1) can be expressed in terms of numerical fluxes as follows:

$$Q_i^{n+1} = Q_i^n - \Delta t_i / V_i \left(VF_1^N + VF_2^N + VF_3^N \right), \tag{70}$$

where VF_1^N, VF_2^N and VF_3^N are the numerical fluxes. For a first order upwind scheme, F_1^N is given by:

$$VF_1^N = F_1^n - \hat{A}_1^+ \Delta_{int} F_i^n, \tag{71}$$

with: $\Delta_{int} = (\cdot)_{ne} - (\cdot)_i$, F_1^n and F_i^n defined by:

$$F_1^n = V_1 \begin{Bmatrix} \rho U_{cont} \\ \rho u U_{cont} + p h_x \\ \rho v U_{cont} + p h_y \\ (e+p) U_{cont} \end{Bmatrix}_1 \quad \text{and} \quad F_i^n = V_i \begin{Bmatrix} \rho U_{cont} \\ \rho u U_{cont} + p h_x \\ \rho v U_{cont} + p h_y \\ (e+p) U_{cont} \end{Bmatrix}_i ; \tag{72}$$

and $\hat{A}_1^+$ defined as follows:

$$\hat{A}_1^+ = \left(R_1 \hat{\Lambda}_1^+ R_1^{-1} \right)_1, \ \hat{\Lambda}_1^+ = \text{diag} \left\{ \hat{\lambda}_1^+ \right\} \quad \text{and} \quad \hat{\lambda}_1^+ = 0.5 \left[1 + \text{sign} \left(\lambda_1^{normal} \right) \right], \tag{73}$$

where: R_1 is defined by Eq. (17) and R_1^{-1} is defined in [23]; $\text{diag}(\cdot)$ represents a diagonal matrix, as for instance:

$$\hat{\Lambda}_\xi^+ = \begin{bmatrix} \hat{\lambda}_1^+ & & & \\ & \hat{\lambda}_2^+ & & \\ & & \hat{\lambda}_3^+ & \\ & & & \hat{\lambda}_4^+ \end{bmatrix}; \tag{74}$$

λ_1^{normal} are defined by Eq. (10) to the normal direction of flux at the l = 1 interface; and $\text{sign}\left(\lambda_1^{normal}\right)$ is equal to 1.0 if $\lambda_1^{normal} \geq 0.0$ and -1.0 otherwise. For explicit methods in the two-dimensional space, the Runge-Kutta method of Eq. (28) is employed with the definition of interface fluxes as described by Eq. (29).

11.2 Uniformly Second Order Essentially Nonoscillatory Schemes

[3] proposed to construct second order accurate TVD schemes by applying a first order approximate Riemann solver to a modified flux. Following [3], [21] proposed to define a modified numerical flux function with the definition of the modified flux:

$$VF^N = F^M = F^n + \overline{F}^n, \tag{75}$$

where VF^M is the modified flux which has essentially nonoscillatory property yet to be defined. In the following, a numerical method of uniformly second order accuracy in time and space which combines both characteristic and conversion features of Eq. (1) is discussed. For the present ENO scheme, the numerical flux VF^N is described by:

$$VF_l^N = F_{i+1}^M - \hat{A}_l^+ \Delta_{int} F_i^M = F_i^M + \hat{A}_l^- \Delta_{int} F_i^M. \tag{76}$$

The components of the additional vector $\overline{F}$ are given by:

$$\bar{f}_i = m\left[\tilde{f}_i + \beta\,\overline{m}\left(\Delta_- \tilde{f}_{i-1}, \Delta_+ \tilde{f}_{i-1}\right), \tilde{f}_{i+1} - \beta\,\overline{m}\left(\Delta_- \tilde{f}_{i+1}, \Delta_+ \tilde{f}_{i+1}\right)\right], \tag{77}$$

where $\Delta_- = (\cdot)_i - (\cdot)_{i-1}$, $\Delta_+ = (\cdot)_{i+1} - (\cdot)_i$, and $\tilde{f}_i$ are components of the following column vector:

$$\tilde{F}_i = \text{sign}(A_l)\left(I - \Delta t_i |A_l|\right)\Delta_{int} F_i / 2. \tag{78}$$

The $\text{sign}(A)$ and $|A|$ in Eq. (78) are given by:

$$\text{sign}(A) = R_{normal}\,\text{diag}\left\{\text{sign}\left(\lambda_i^{normal}\right)\right\}R_{normal}^{-1} \quad \text{and} \quad |A| = R_{normal}\,\text{diag}\left\{\left|\lambda_i^{normal}\right|\right\}R_{normal}^{-1}, \tag{79}$$

where R_{normal} and R_{normal}^{-1} are the matrices defined by Eq. (17) and [23], respectively. In Equation (77), m is the minmod function:

$$m(a,b) = s \times \min\left(|a|, |b|\right), \quad \text{if sign(a) = sign(b) = s;} \tag{80}$$

$$m(a,b) = 0.0, \text{ otherwise.} \tag{81}$$

and the $\overline{m}$ function is defined by:

$$\overline{m} = a, \quad \text{if } |a| \le |b|; \tag{82}$$

$$\overline{m} = b, \quad \text{if } |a| \ge |b|. \tag{83}$$

For β = 0.0, one has a second order TVD scheme. For β = 0.5, one has a uniformly second order nonoscillatory scheme. The numerical scheme is thus formed by Eq. (70) using the definition (76) to the numerical flux function and the explicit time integration is performed by the Runge-Kutta method described by Eq. (28).

The first author introduced some modifications in the [21] scheme. Equation (76) is redefined:

$$VF_l^N = F_{i+1}^M - A_l^+ \Delta_{int} Q_i^M = F_i^M + A_l^- \Delta_{int} Q_{i,}^M, \tag{84}$$

with: $F_{i+1}^{M} = F_{i+1}^{n} + A_l^{n}\overline{F}_{i+1}^{n}$ and $Q_i^{M} = V_{int}\{\rho \quad \rho u \quad \rho v \quad e\}_i^{T} + \overline{F}_i^{n}$. The positive splitting matrix A_l^{+} is defined as

$$A_l^{+} = R_{normal}\,\mathrm{diag}\{\lambda_l^{+}\}R_{normal}^{-1}, \tag{85}$$

with $\lambda_l^{+} = 0.5\left(\lambda_l^{normal} + \left|\lambda_l^{normal}\right|\right)$, and the Jacobian matrix at the normal flux direction is described by

$$A_l^{n} = R_{normal}\,\mathrm{diag}\{\lambda_l^{normal}\}R_{normal}^{-1}. \tag{86}$$

The vector $\widetilde{F}_i$ is also redefined as:

$$\widetilde{F}_i = \mathrm{sign}(A_l)\left(I - \Delta t_i\left|A_l\right|\right)\Delta_{int}\,Q_i/2, \tag{87}$$

where $Q_i = V_{int}\{\rho \quad \rho u \quad \rho v \quad e\}_i^{T}$ is the vector of conserved variables in the cell "i".

Observe that the resulting schemes are equivalent to the originals of [21], with the unique difference that the difference of fluxes in Eq. (76) is changed by the difference of conserved variable values, Eq. (84). With this new definition, the solutions present better behavior, free of oscillations, undershoots and overshoots. The other expressions maintain the same structure.

12 Yang and Hsu (1992) UNO Algorithm

The [22] UNO scheme is equivalent to an ENO scheme of third order of accuracy. The components of φ_i^{UNO3} are defined as:

$$\varphi_i^{UNO3} = \sigma(\lambda_i^m)(\beta_i^m + \beta_{i+1}^m) + \begin{cases} \overline{\sigma}(\lambda_i^m)(\overline{\beta}_i^m + \overline{\beta}_{i+1}^m) - \psi(\lambda_i^m + \gamma_i^m + \overline{\gamma}_i^m)\alpha_i^m, & \text{if} \quad \left|\alpha_{i-1}^m\right| \le \left|\alpha_i^m\right| \\ \hat{\sigma}(\lambda_i^m)(\hat{\beta}_i^m + \hat{\beta}_{i+1}^m) - \psi(\lambda_i^m + \gamma_i^m + \hat{\gamma}_i^m)\alpha_i^m, & \text{if} \quad \text{otherwise} \end{cases}; \tag{88}$$

where the $\sigma, \overline{\sigma}, \text{and } \hat{\sigma}$ functions are given by:

$$\sigma = \frac{1}{2}\left[\psi(z) - \lambda z^2\right]; \quad \overline{\sigma} = \frac{1}{6}\left[2|z| - 3\lambda|z|^2 + \lambda^2|z|^3\right]; \quad \text{and} \quad \hat{\sigma} = \frac{1}{6}\left[\lambda^2|z|^3 - |z|\right]. \tag{89}$$

The $\beta, \overline{\beta}, \text{and } \hat{\beta}$ are parameters defined by:

$$\beta = m[\alpha_i^m, \alpha_{i-1}^m]; \tag{90}$$

$$\overline{\beta} = \overline{m}\left[\Delta_-\alpha_{i-1}^m, \Delta_+\alpha_{i-1}^m\right] \quad \text{if} \quad \left|\alpha_{i-1}^m\right| \le \left|\alpha_i^m\right|; \tag{91}$$

$$\hat{\beta} = \overline{m}\left[\Delta_-\alpha_i^m, \Delta_+\alpha_i^m\right] \quad \text{if} \quad \left|\alpha_{i-1}^m\right| > \left|\alpha_i^m\right|. \tag{92}$$

and finally, the γ, $\bar{\gamma}$, and $\hat{\gamma}$ numerical speed of propagation of information are given by:

$$\gamma = \sigma(\lambda_i^m)\begin{cases}\left(\beta_{i+1}^m - \beta_i^m\right)/\alpha^m & \text{if} \quad \left|\alpha^m\right| \neq 0.0; \\ 0.0 & \text{otherwise}\end{cases} \tag{93}$$

$$\bar{\gamma} = \bar{\sigma}(\lambda_i^m)\begin{cases}\left(\bar{\beta}_{i+1}^m - \bar{\beta}_i^m\right)/\alpha^m & \text{if} \quad \left|\alpha^m\right| \neq 0.0; \\ 0.0 & \text{otherwise}\end{cases} \tag{94}$$

$$\hat{\gamma} = \hat{\sigma}(\lambda_i^m)\begin{cases}\left(\hat{\beta}_{i+1}^m - \hat{\beta}_i^m\right)/\alpha^m & \text{if} \quad \left|\alpha^m\right| \neq 0.0; \\ 0.0 & \text{otherwise}\end{cases} \tag{95}$$

Finally, the dissipation operator of [22], to third order of spatial accuracy, in its UNO version, is constructed by the following matrix-vector product:

$$\left\{D_{\text{Yang/Hsu}}\right\}_l = \left[R\right]_l \left\{\varphi^{\text{UNO3}}\right\}_l . \tag{96}$$

The complete numerical flux vector to the "l" interface is described by Eqs. (26), (27), and (29) whereas the tine integration is performed by the Runge-Kutta method of Eq. (28).

13 Spatially Variable Time Step

The basic idea of this procedure consists in keeping constant the CFL number in all calculation domain, allowing, hence, the use of appropriated time steps to each specific mesh region during the convergence process. According to the definition of the CFL number, it is possible to write:

$$\Delta t_i = \text{CFL}\left(\Delta s\right)_i / c_i , \tag{97}$$

where CFL is the "Courant-Friedrichs-Lewy" number to provide numerical stability to the scheme; $c_i = \left[\sqrt{u^2 + v^2} + a\right]_i$ is the maximum characteristic speed of propagation of information in the calculation domain; and $\left(\Delta s\right)_i$ is a characteristic length of transport of information. On a finite volume context, $\left(\Delta s\right)_i$ is chosen as the minor value found between the minor centroid distance, involving the i cell and a neighbor, and the minor cell side length.

14 Physical Problems

The first problem to be studied is the transonic convergent-divergent nozzle. The geometry of the convergent-divergent nozzle at the xy plane is described in Fig. 2. The total length of the nozzle is 0.38ft (0.116m) and the throat height is equal to 0.090ft (0.027m). The throat is located at 0.19ft (0.058m) from the entrance boundary. The throat curvature ratio is equal to 0.090ft. The nozzle convergence angle is 22.33° and the nozzle divergence angle is 1.21°. An exponential stretching of 10% in both normal and tangent lines was used. An algebraic mesh of 61 points in the tangent direction and 71 points in the normal direction was generated, which corresponds in finite volumes to 8,400 triangular cells and 4,331 nodes. Fig. 3 exhibits the mesh employed in the simulations.

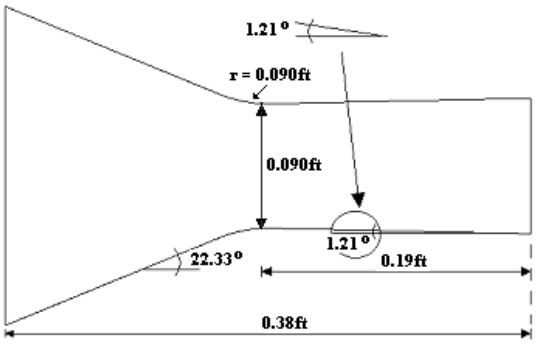

Fig. 2. Nozzle configuration at the xy plane.

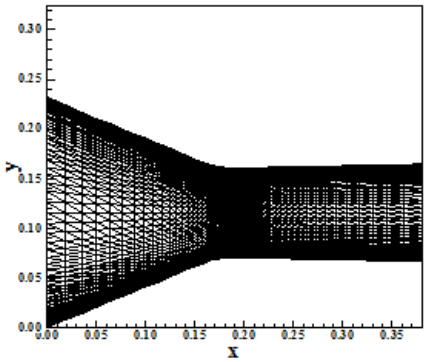

Fig. 3. Nozzle mesh in two-dimensions.

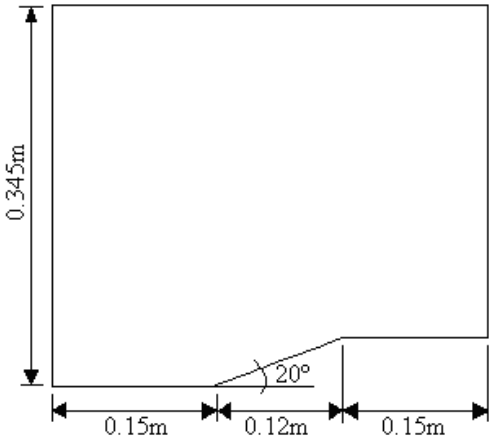

Fig. 4. Ramp configuration at the xy plane.

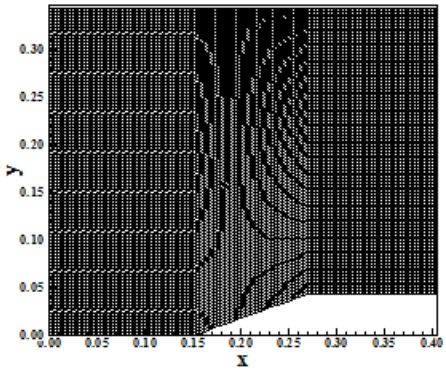

Fig. 5. Ramp mesh in two-dimensions.

The second problem is the ramp problem. The ramp configuration at the xy plane is described in Fig. 4. The compression corner has 20° of inclination. The mesh used in the simulations has 11,880 triangular cells and 6,100 nodes to a structured discretization of the calculation domain. This mesh is equivalent, in finite differences, of being composed of 61 points in the tangent direction and 100 points in the normal direction. Fig. 5 shows such mesh. The initial and boundary conditions are described in [25].

15 Results

15.1 Nozzle problem

Figs. 6 and 7 exhibit the pressure and Mach number contours generated by the [6] scheme. Both pressure and Mach number contours are of good quality. The weak shock wave at the nozzle throat is well captured by the [6] scheme.

Figs. 8 and 9 show the pressure and Mach number contours generated by the [3] scheme. The pressure and Mach number contours are of good quality. The shock wave at the nozzle throat is accurately captured by the [3] scheme.

Figs. 10 and 11 present the pressure and Mach number contours obtained by the [7] scheme. The pressure contours are of good quality, but the Mach number contours are worse than the respective ones obtained by the other schemes. The weak shock wave is well captured by this scheme.

Figs. 12 and 13 exhibit the pressure and Mach number contours obtained by the [8] scheme. The pressure and Mach number contours are of good quality. The weak shock wave at the throat is well captured by the [8] scheme.

Figs. 14 and 15 show the pressure and Mach number generated by the [9] scheme as using the Eq. (44) to the function Q. Both pressure and Mach number are of good quality and the weak shock wave at the throat is well captured.

Figs. 16 and 17 present the pressure and Mach number contours calculated with the [10] scheme. The pressure and Mach number contours are of good quality, comparable to [9]. The weak shock wave at the throat is also captured.

Figs. 18 and 19 exhibit the pressure and Mach number contours obtained by the [11] scheme. The pressure and Mach number contours are of good quality, the best until now. The weak shock wave at the nozzle throat is well captured by this scheme.

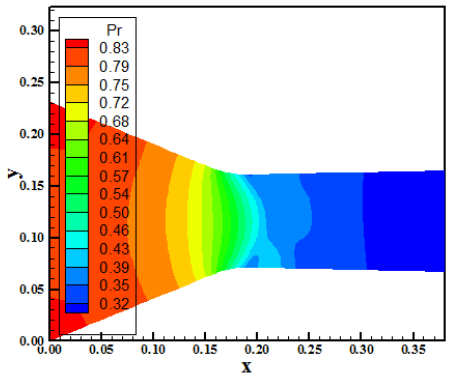

Fig. 6. Pressure contours ([6]).

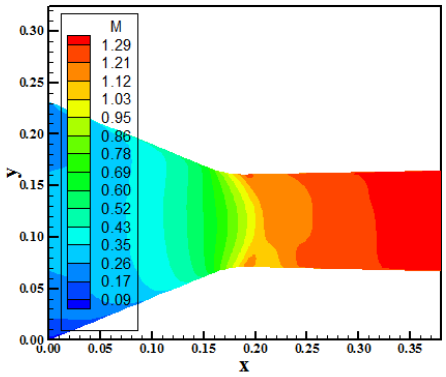

Fig. 7. Mach number contours ([6]).

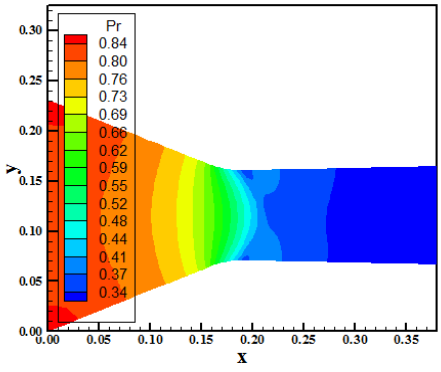

Fig. 8. Pressure contours ([3]).

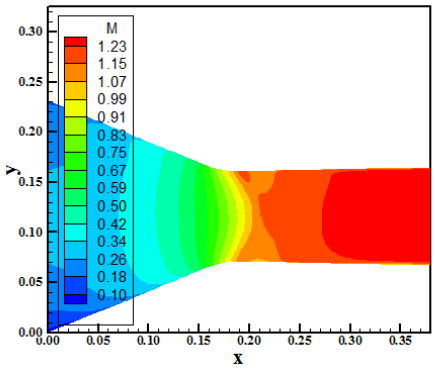

Fig. 9. Mach number contours ([3]).

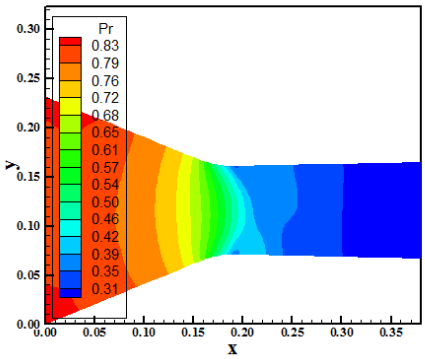

Fig. 10. Pressure contours ([7]).

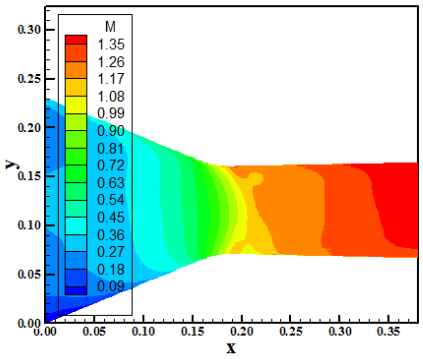

Fig. 11. Mach number contours ([7]).

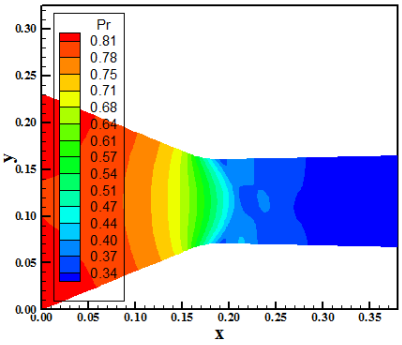

Fig. 12. Pressure contours ([8]).

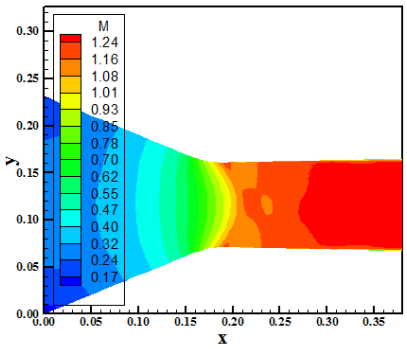

Fig. 13. Mach number contours ([8])

Figs. 20 and 21 present the pressure and Mach number contours generated by the [13] TVD scheme. The pressure and Mach number contours are of good quality, very similar with the solutions of the [9] scheme. Figs. 22 and 23 show the pressure and Mach number generated by the [13] ENO scheme. The solutions are of good quality, similar to the [9] scheme solution.

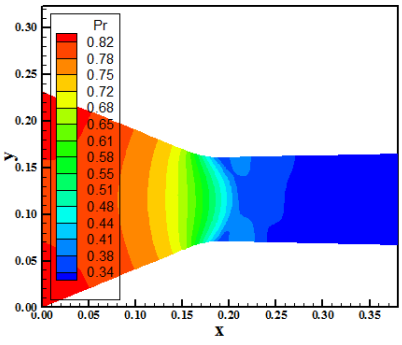

Fig. 14. Pressure contours ([9]).

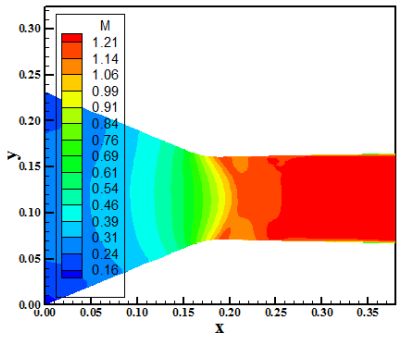

Fig. 15. Mach number contours ([9]).

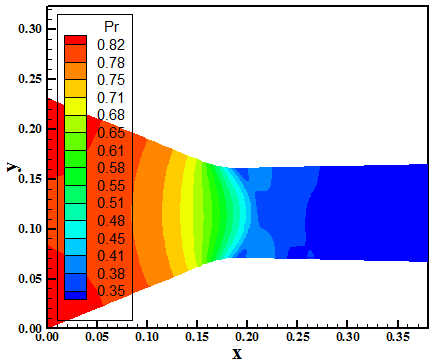

Fig. 16. Pressure contours ([10]).

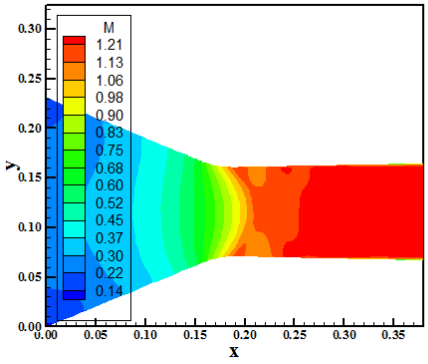

Fig. 17. Mach number contours ([10]).

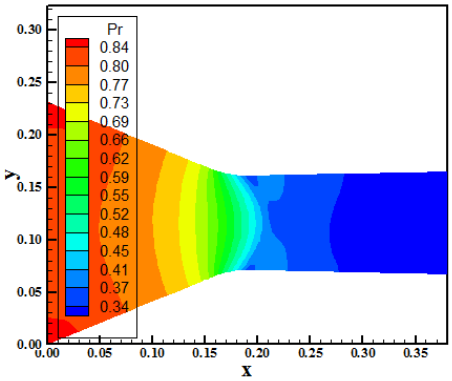

Fig. 18. Pressure contours ([11]).

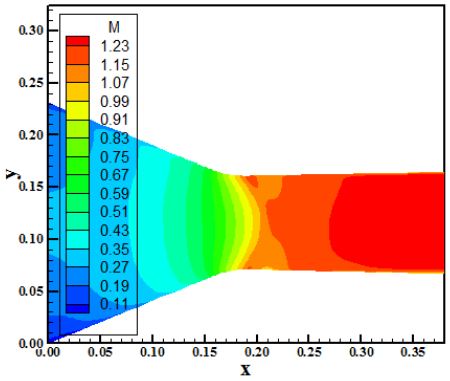

Fig. 19. Mach number contours ([11]).

Figs. 24 and 25 present the pressure and Mach number contours obtained by the [21] scheme in its TVD version. The ENO version of this algorithm did not present converged solutions. The pressure contours are of good quality, but the Mach number contours are badly described. The weak shock at the nozzle throat is well captured by the pressure contours.

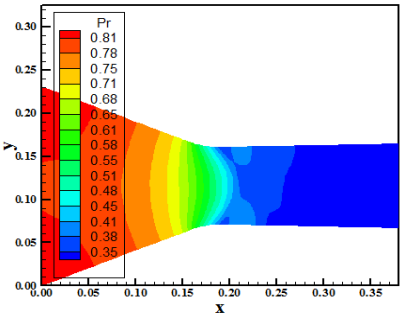

Fig. 20. Pressure contours ([13]-TVD).

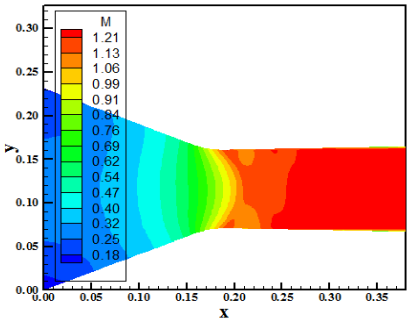

Fig. 21. Mach number contours ([13]-TVD).

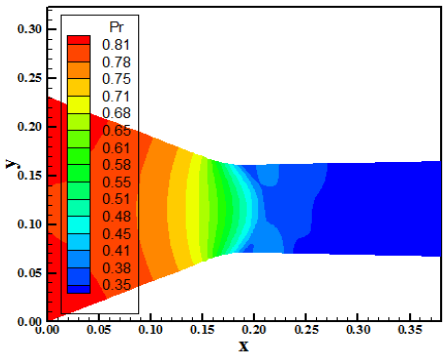

Fig. 22. Pressure contours ([13]-ENO).

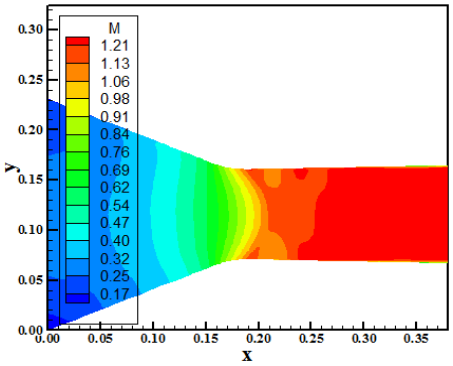

Fig. 23. Mach number contours ([13]-ENO).

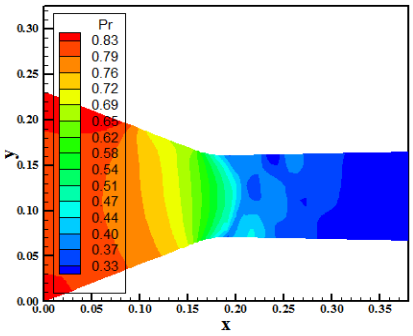

Fig. 24. Pressure contours ([21]-TVD).

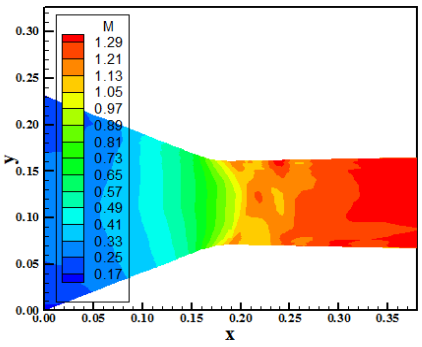

Fig. 25. Mach number contours ([21]-TVD).

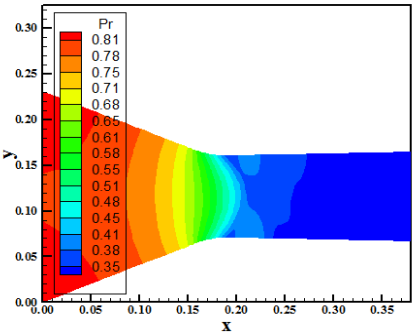

Fig. 26. Pressure contours ([22]).

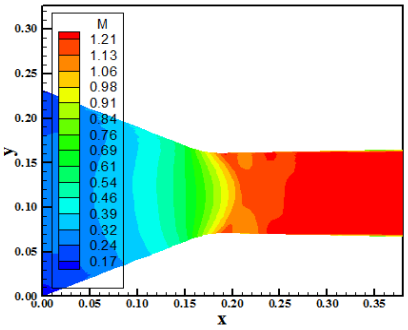

Fig. 27. Mach number contours ([22]).

Figs. 26 and 27 show the pressure and Mach number contours generated by the [22] scheme. This UNO algorithm yields good solutions to the pressure and Mach number contours. The weak shock wave is well captured.

Finally, Fig. 28 presents the wall pressure ratio calculated by all ten schemes. The pressure distributions are compared with the experimental results of [26]. The best wall pressure distribution is due to [21] in its TVD version.

15.2 Ramp problem

For this problem, a supersonic Mach number of 2.0 and an entrance angle of 0.0^{o} were employed as initial condition.

Figs. 29 and 30 exhibit the pressure and Mach number contours obtained by the [6] scheme. The shock wave and the expansion fan are appropriately captured by the numerical algorithm. The curves of contours are of good quality, although the Mach contours present some oscillations close to the shock, the pre-shock oscillations.

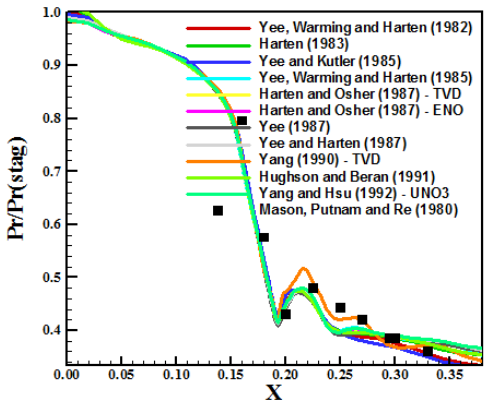

Fig. 28. Wall pressure distributions (Choosing the best distribution)

Figs. 31 and 32 show the pressure and Mach number contours calculated by the [3] scheme. Both solutions present good contours of pressure and of Mach number. The Mach number field is free of pre-shock oscillations. Both solutions have good homogeneity properties.

Figs. 33 and 34 present the pressure and Mach number contours generated by the [7] scheme. Both solutions are of good quality, although the Mach number contours present some pre-shock oscillations.

Figs. 35 and 36 exhibit the pressure and Mach number contours obtained by the [8] scheme. Some pre-shock oscillations are observed in the Mach number contours. The pressure field is free of oscillations and the shock wave is well captured.

Figs. 37 and 38 show the pressure and Mach number contours calculated by the [13] scheme in its TVD version. The shock is captured with formation of some pre-shock oscillations. The pressure field is better captured, without oscillations. Figs. 39 and 40 present the pressure and Mach number contours generated by [13] scheme in its ENO version. The Figs. are very similar to the respective ones of the TVD case. A line of pre-shock oscillations is observed along the shock. The pressure contours are well defined.

Figs. 41 and 42 exhibit the pressure and Mach number contours obtained with the [9] scheme using Eq. (44) as the limiter. Both contours are well captured, characterizing the [3] and the [9] as the best one until now. The shock wave is well captured by the [9] scheme.

Figs. 43 and 44 show the pressure and the Mach number contours generated by the [10] scheme. The pressure contours are of good quality, but the Mach number contours present the same behavior as in the [13] solutions.

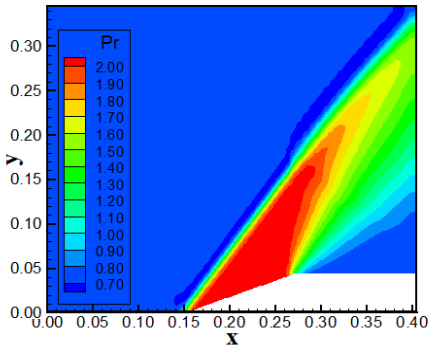

Fig. 29. Pressure contours ([6]).

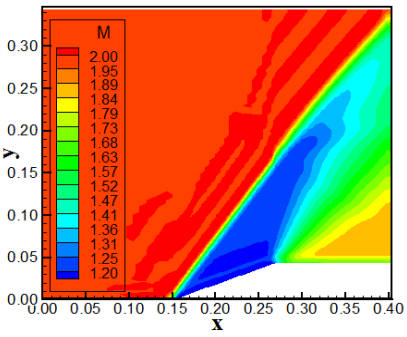

Fig. 30. Mach number contours ([6]).

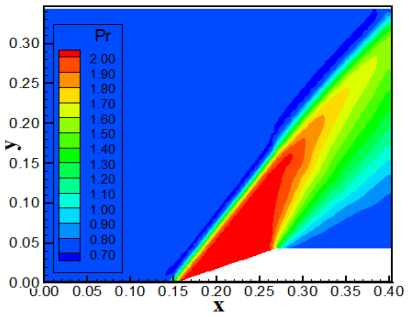

Fig. 31. Pressure contours ([3]).

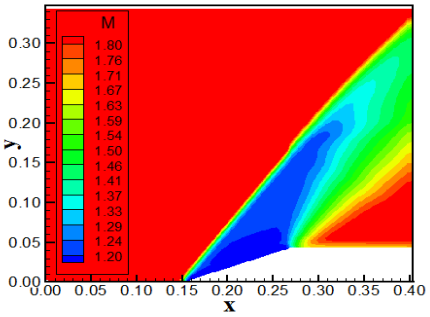

Fig. 32. Mach number contours ([3]).

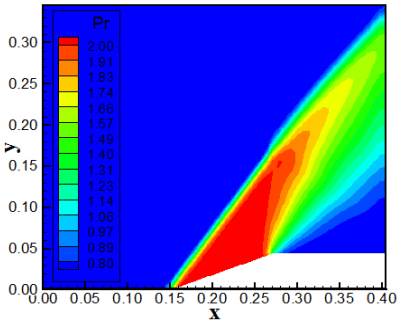

Fig. 33. Pressure contours ([7]).

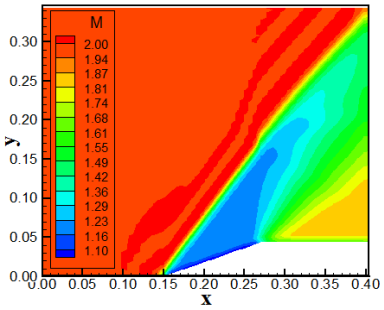

Fig. 34. Mach number contours ([7]).

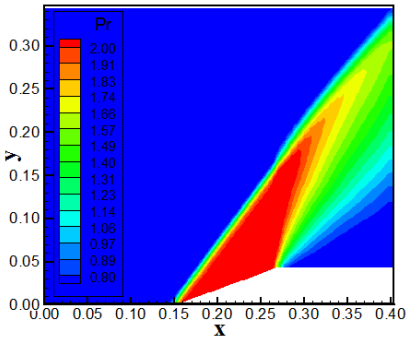

Fig. 35. Pressure contours ([8]).

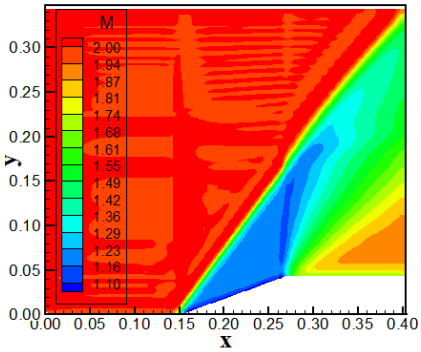

Fig. 36. Mach number contours ([8]).

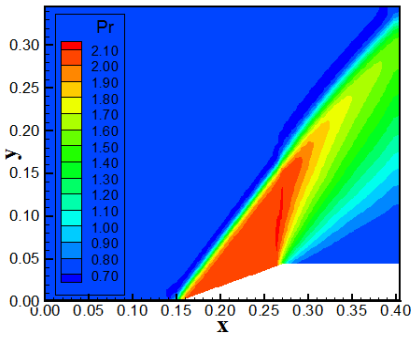

Fig. 37. Pressure contours ([13]-TVD).

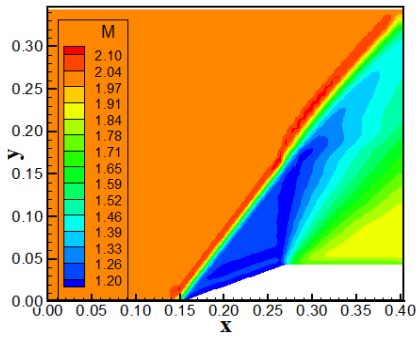

Fig. 38. Mach number contours ([13]-TVD).

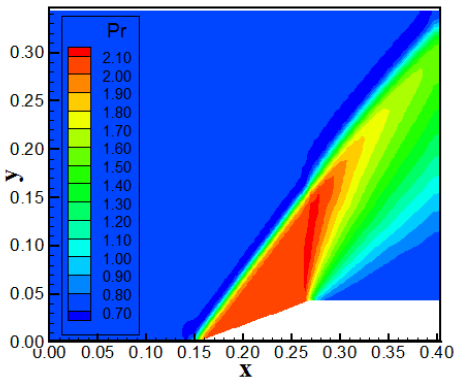

Fig. 39. Pressure contours ([13]-ENO).

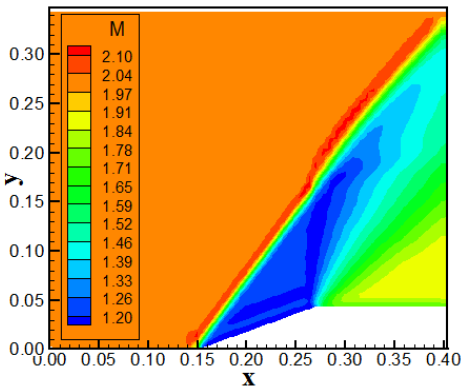

Fig. 40. Mach number contours ([13]-ENO).

Figs. 45 and 46 present the pressure and Mach number contours obtained by the [11] scheme. The Mach number contours present some pre-shock oscillations, but the pressure contours are free of such instabilities.

Figs. 47 and 48 exhibit the pressure and Mach contours generated by the [21] scheme. Both pressure and Mach number contours are badly captured. The shock wave is badly estimated. Oscillations along the shock wave are perceptible in the Mach number contours.

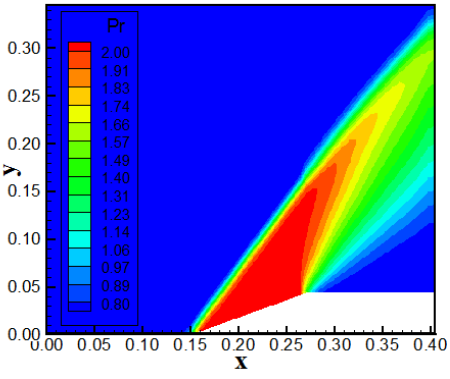

Fig. 41. Pressure contours ([9]).

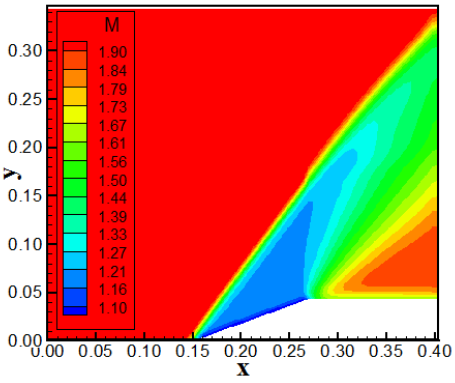

Fig. 42. Mach number contours ([9]).

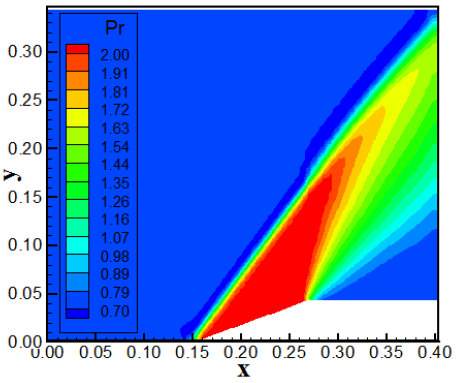

Fig. 43. Pressure contours ([10]).

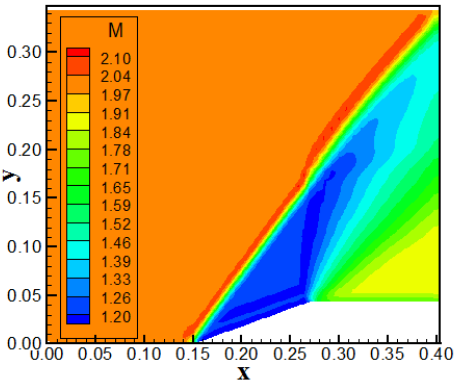

Fig. 44. Mach number contours ([10]).

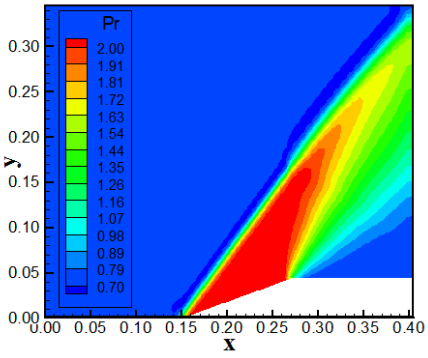

Fig. 45. Pressure contours ([11]).

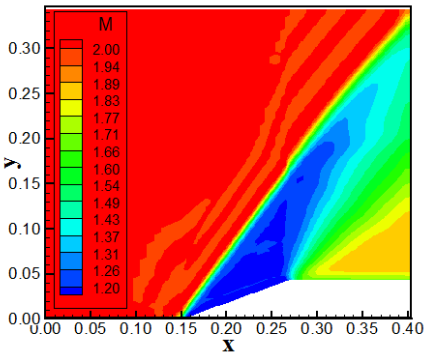

Fig. 46. Mach number contours ([11]).

Figs. 49 and 50 present the pressure and the Mach number contours calculated with the [22] scheme. The similar behavior of the [13] scheme is observed in these solutions. A line of pre-shock oscillations is captured along the oblique shock wave.

Fig. 51 shows the wall pressure distributions obtained with the TVD schemes, where the [10] and [11] solutions were the best, and 52 shows the wall pressure distributions obtained with the ENO schemes, where the [13]'s solutions in both variants were the best. The best distribution of each one is compared in Fig. 53 and the best distribution is exhibited in Fig. 54. In this study, the best wall pressure distribution is due to [13] to both TVD and ENO variants.

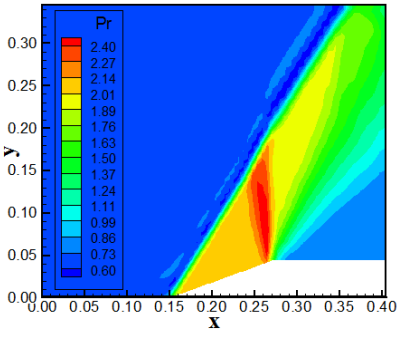

Fig. 47. Pressure contours ([21]).

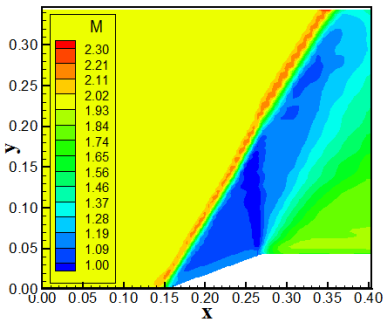

Fig. 48. Mach number contours ([21]).

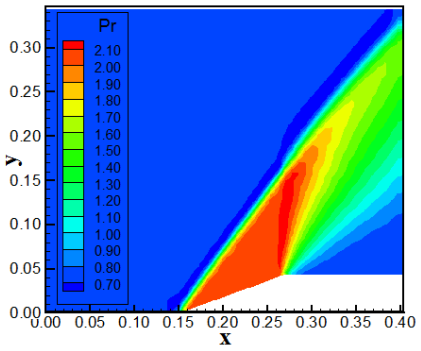

Fig. 49. Pressure contours ([22]).

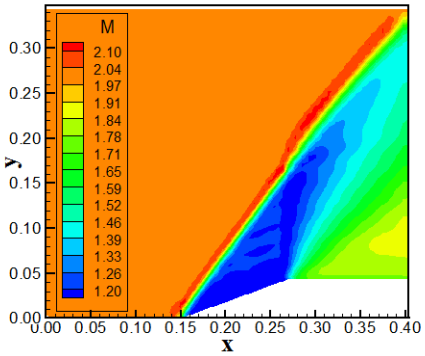

Fig. 50. Mach number contours ([22]).

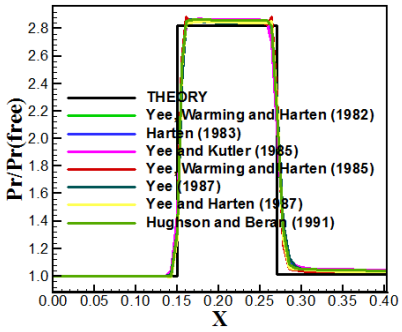

Fig. 51. Wall pressure distributions (TVD).

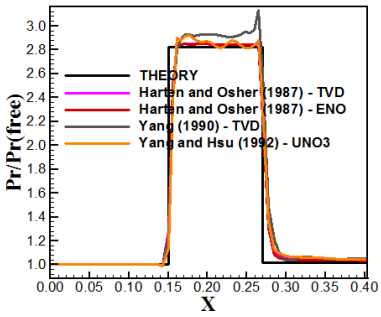

Fig. 52. Wall pressure distributions (ENO).

A way to quantitatively verify if the solutions generated by each scheme are satisfactory consists in determining the shock angle of the oblique shock wave, β, measured in relation to the initial direction of the flow field. [27] presents a diagram with values of the shock angle, β, to oblique shock waves. The value of this angle is determined as function of the freestream Mach number and of the deflection angle of the flow after the shock wave, ϕ. To ϕ = 20º (ramp inclination angle) and to a freestream Mach number equals to 2.0, it is possible to obtain from this diagram a value to β equals to 53.0º. Using a transfer in all pressure contours figures, it is possible to obtain the values of β to each scheme, as well the respective errors, shown in Tab. 2. As can be noted, the best results are due to [6], [9], [10], and [13] (in both TVD and ENO variants) with an error of 0.00%. Hence, in this supersonic problem, the [13], in both TVD and ENO versions, was the best.

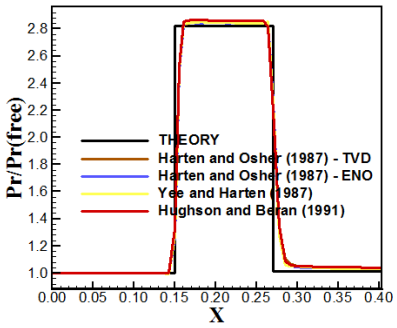

Fig. 53. Wall pressure distributions (Choosing the best profile).

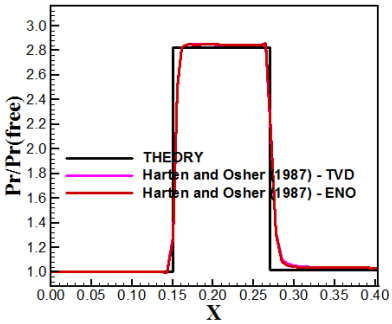

Fig. 54. Wall pressure distributions (The best profiles).

Table 2. Shock angle and percentage errors

Scheme	β (°)	Error (%)
Yee, Warming and Harten (1982), [6]	53.0	0.00
Harten (1983), [3]	54.0	1.89
Yee and Kutler (1985), [7]	54.0	1.89
Yee, Warming and Harten (1985), [8]	53.3	0.57
Harten and Osher (1987), [13] – TVD	53.0	0.00
Harten and Osher (1987), [13] – ENO	53.0	0.00
Yee (1987), [9]	53.0	0.00
Yee and Harten (1987), [10]	53.0	0.00
Yang (1990) – TVD	58.0	9.43
Hughson and Beran (1991)	53.4	0.75
Yang and Hsu (1992) – UNO3	53.4	0.75

16 Conclusions

In this work, the Euler equations in two-dimensions were solved by the use of TVD, ENO and UNO schemes, second and third order accurate. The following ten flux difference splitting algorithms were employed: [6,3,7-11], on a TVD approach, [13,21], on an ENO approach, and finally [22], on a UNO approach. A finite volume formulation was employed on conservative and unstructured contexts. The time discretization employed a Runge-Kutta method of five steps. All ten algorithms were applied to the solution of two problems: the transonic convergent-divergent symmetrical nozzle, and the supersonic ramp. All schemes were accelerated to the steady state solution using a spatially variable time step procedure, which had proved excellent characteristics of convergence [24-25]. The results have demonstrated that the best result of the wall pressure distribution in the nozzle case was due to [21] and the best wall pressure distribution and shock angle in the ramp case was due to [13] to its both TVD and ENO versions.

The merit of this study was to highlight the [13] scheme, in both TVD and ENO versions, and the [21] scheme as able to capture the main aspects of the flow field and, in the case of supersonic flow, to capture the shock wave with accuracy. Moreover, the implementation of these schemes on an unstructured context is also a significant and important contribution to the CFD community.

The new algorithm developed by the first author is easy to work and present the possibility of using 10 different numerical schemes for solving the fluid flow. They were implemented on both two- and three-dimensional contexts. They are implemented on a cell centered database. It can use different time step procedures, one for inviscid flows and another for viscous flows. It needs more elaboration on grid refinement, but for simple geometries it works well. Grid refinement is the next step to improve the algorithm. In relation to existing ones, it is comparable in computational cost, being cheaper than the others because of the grid refinement absence, and presents solutions as good as the others.

Finally, together with grid refinement, the focus of new works are concentrated in more high order unstructured schemes to evaluation and to study error estimation. With this in mind some new references are cited here as promising in such areas: [28-33].

Acknowledgements

The first author would like to thank CAPES by the scholarship which permitted the accomplishment of this work. He also thanks the ITA by the infra-structure that also allowed the realization of this work.

Competing Interests

Authors have declared that no competing interests exist.

References

[1] Richtmeyer RD, Morton KW. Difference Methods for Initial-Value Problem, Interscience-Wiley, New York; 1967.

[2] Harten A. On a class of high resolution total-variation-stable finite-difference schemes. NYU Report, New York University, New York, October; 1982.

[3] Harten A. High resolution schemes for hyperbolic conservation laws. Journal of Computational Physics. 1983;49(2):357-393.

[4] Harten A, Hyman JM, Lax PD. Commun. Pure Appl. Math. 1976;29:297.

[5] Crandall MG, Majda A. Math. Comput. 1980;34(149):1.

[6] Yee HC, Warming RF, Harten A. A high-resolution numerical technique for inviscid gas-dynamic problems with weak solutions. Proceedings of the 8th International Conference on Numerical Methods in Fluid Dynamics, E. Krause, Editor, Lecture Notes in Physics. Springer-Verlag, Berlim, Germany. 1982;170:546-552.

[7] Yee HC, Kutler P. Application of second-order-accurate total variation diminishing (TVD) Schemes to the euler equations in general coordinates. NASA-TM-85845; 1985.

[8] Yee HC, Warming RF, Harten A. Implicit total variation diminishing (TVD) schemes for steady-state calculations. Journal of Computational Physics. 1985;57(3):327-360.

[9] Yee HC. Construction of explicit and implicit symmetric tvd schemes and their applications. Journal of Computational Physics. 1987;68:151-179.

[10] Yee HC, Harten A. Implicit TVD schemes for hyperbolic conservation laws in curvilinear coordinates. AIAA Journal. 1987;25(2):266-274.

[11] Hughson MC, Beran PS. Analysis of hyperbolic blunt-body flows using a total variations diminishing (TVD) scheme and the maccormack scheme. AIAA 91-3206-CP.

[12] Yee HC. A class of high-resolution explicit and implicit shock-capturing methods. NASA TM-101088; 1989.

[13] [13] Harten A, Osher S. Uniformly high order accurate non-oscillatory schemes. SIAM J. Num. Anal. 1987;24(2):279-309.

[14] Harten A, Engquist B, Osher S, Chakravarthy SR. Uniformly High order accurate essentially non-oscillatory schemes. II"., Preprint; 1986.

[15] Harten A, Engquist B, Osher S, Chakravarthy SR. Some results on uniformly high order accurate essentially non-oscillatory schemes. Advances in Numerical Analysis and Applied Mathematics, edited by J. C. South, Jr. and M. Y. Hussaini, ICASE Rept. 86-18; also Journal of Applied Num. Mathematics. 1986;2:347-367.

[16] Harten A, Engquist B, Osher S, Chakravarthy SR. Uniformly high order accurate essentially non-oscillatory schemes. III. ICASE Rept. 1986;86-22.

[17] Godunov SK. A difference scheme for numerical computation of discontinuous solution of hydrodynamic equations. Math. Sbornik. 1958;47:271-306.

[18] Colella P, Woodward PR. The piecewise-parabolic method (PPM) for gas-dynamics simulation. Journal of Computational Physics. 1984;54(1):174-201.

[19] Van Leer B. Towards the ultimate conservative difference scheme. V. A second order sequel to Godunov's method. Journal of Computational Physics. 1979;32:101-136.

[20] Osher S, Chakravarthy SR. High resolution schemes and entropy conditions. SIAM Journal of Numerical Analysis. 1984;21(4):955-984.

[21] Yang JY. Uniformly second-order-accurate essentially nonoscillatory schemes for the euler equations. AIAA Journal. 1990;28(12):2069-2076.

[22] Yang JY, Hsu CA. High-resolution, nonoscillatory schemes for unsteady compressible flows. AIAA Journal. 1992;30(6):1570-1575.

[23] Maciel ESG. Simulations in 2D and 3d applying unstructured algorithms, euler and navier-stokes equations – perfect gas formulation. Saarbrücken, Deutschland: Lambert Academic Publishing (LAP), 2015;Ch. 1:26-47.

[24] Maciel ESG. Simulations in 2D and 3D applying unstructured algorithms, euler and navier-stokes equations – perfect gas formulation. Saarbrücken, Deutschland: Lambert Academic Publishing (LAP). 2015;Ch. 6:160-181.

[25] Maciel ESG, Ferreira EM. Applications of TVD and ENO Algorithms in 2D and 3D, euler and navier-stokes equations. Saarbrücken, Deutschland: Lambert Academic Publishing (LAP); 2015.

[26] Mason ML, Putnam LE, Re RJ. The effect of throat contouring on two-dimensional converging-diverging nozzles at sonic conditions. NASA Technical Paper 1704; 1980.

[27] Anderson Jr. JD. Fundamentals of aerodynamics. McGraw-Hill, Inc., 5th Edition. 2010;1008.

[28] Zhang S, Zhao X. High order data reconstruction schemes for unstructured grid. AIAA Paper 2006-3061; 2006.

[29] Phillips TS, Roy CJ. Residual methods for discretization error estimation. AIAA Paper 2011-3870; 2011.

[30] Zhao Q, Sheng C. Improvements of high-order unstructured grid schemes through RBF interpolation-II. AIAA Paper 2012-0727; 2012.

[31] Yan GKK, Puneria VP, Jalali A, Olliver-Gooch C. Truncation and discretization error for diffusion schemes on unstructured meshes. *AIAA Paper 2014-0478;* 2014.

[32] Hartmann R, Leicht T. High-order unstructured grid generation and discontinous galerkin discretization applied to a 3D high-lift configuration. AIAA Paper 2015-0819; 2015.

[33] Kozubskaya T, Bakhvalov P. On efficient vertex-centered schemes on hybrid unstructured meshes. AIAA Paper 2016-2966; 2016.

Peer-review history:
The peer review history for this paper can be accessed here (Please copy paste the total link in your browser address bar)
http://sciencedomain.org/review-history/21451